Tribology International 164 (2021) 107234

Contents lists available at ScienceDirect

Tribology International

journal homepage: www.elsevier.com/locate/triboint

On the retraction of an adhesive cylindrical indenter from a viscoelastic substrate

Jan Steven Van Dokkum [a], Francesc Pérez-Ràfols [b,*], Leonid Dorogin [b], Lucia Nicola [a,b]

[a] Department of Materials Science and Engineering, Delft University of Technology, 2628CD Delft, The Netherlands
[b] Department of Industrial Engineering, University of Padova, 35131 Padua, Italy

ARTICLE INFO

Keywords:
Adhesion contact
Indentation
Line contact
Boundary Element Method

ABSTRACT

The retraction of a cylindrical rigid indenter from a viscoelastic substrate is studied by means of an efficient Green's function method. Hysteresis is observed in the load to area relationship in accordance with experimental results. Although our model relaxes many assumptions posed by LEFM-based analytical theories, the results fall between the limits, at high and low retraction velocities, predicted by the theories. Approaching the high velocity instantaneous limit requires, however, very high velocities or Maugis parameter. The work of adhesion is found to change during retraction. A non-dimensional parameter is proposed to estimate the effect of viscoelasticity in adhesive hysteresis.

1. Introduction

The contact mechanics of rubbers is relevant in various applications, which include tires [1,2], pressure sensitive adhesives [3,4], and conveying belts [5]. In order to understand how rubber behaves in contact, several research groups have studied the behaviour of glass balls when pressed against a PDMS flat surface [6–9–12–15]. Upon indentation and retraction, these studies reveal hysteresis in the load-to-area response. Indeed, while the indentation curve tends to align closely with the curve predicted by the JKR theory of adhesion [16], there is a deviation upon retraction, as the contact area decreases slower than load. This hysteresis is usually described through a change in the apparent work of adhesion, which is larger during retraction than during indentation. There is, however, an ongoing discussion in the literature regarding the physical origin of hysteresis. The common use of an apparent work of adhesion to describe the hysteresis in those works suggests that it is expected to arise at or near the interface, rather than at the bulk of the material. One should note, however, that if the indentation and retraction are carried at velocities much higher than those studied in the aforementioned works, bulk viscoelasticity could also become relevant. The model presented in this work is appropriate at any speed since it captures both bulk and near-surface viscoelasticity. Several causes have been identified to explain the hysteresis, which include roughness [15,17], mechanical instabilities [6,18], the nature of chemical bonding [6–8], molecular entanglement [18], and viscoelasticity [12,13,18,19]. Likely, all of these have an effect and experimental conditions dictate what dominates.

In this work, we model the adhesive smooth contact between a rigid and a viscoelastic body through simulations, where the only source of hysteresis is the viscoelastic dissipation in the presence of adhesion. Greenwood and Johnson [19] showed that, if the retraction is slow enough so that the bulk stresses can be related to the deformation through the relaxed modulus, the change in response due to viscoelasticity is equivalent to that obtained through a change in the work of adhesion. As reported in [19], a standard application LEFM, allowing for a stress singularity at the edge of the contact, implies that viscoelastic effects are fully developed even at infinitesimal velocities and hence that no velocity dependence exist. Hence, a more complex analysis, considering the crack shape in detail, is required. Such analysis led the authors to obtain a relation between the work of adhesion and the opening velocity, but not between the contact area and load. The relation between work of adhesion and velocity in an opening crack was also studied by Persson and Brener [20] and Carbone and Persson [21], who gave a more detailed solution. Again, they provided only a relation between opening velocity and work of adhesion. Barthel and Frétigny [22] did provide load to area relations for the case of a ball-on-flat contact. Unfortunately, the model does not extend easily to the cylinder-on-flat contact, which will be the focus of this work.

In this work, we advance fundamental knowledge on the interplay between adhesion and viscoelasticity on adhesional hysteresis by

* Corresponding author.
E-mail address: francisco.perezrafols@unipd.it (F. Pérez-Ràfols).

https://doi.org/10.1016/j.triboint.2021.107234
Received 22 March 2021; Received in revised form 10 August 2021; Accepted 11 August 2021
Available online 16 August 2021

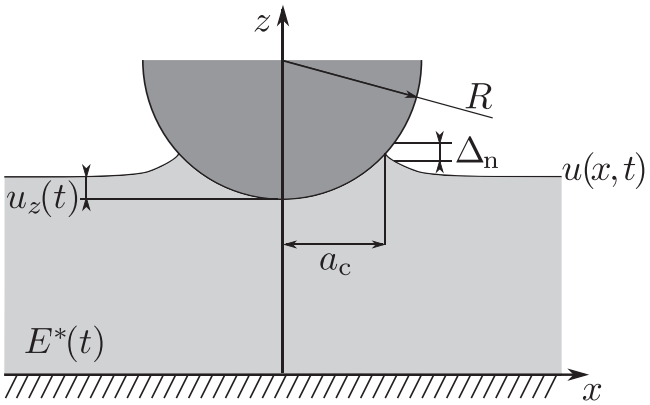

Fig. 1. Schematic representation of the adhesive contact of a rigid smooth cylindrical indenter with radius R on the viscoelastic substrate. Here, ac is the contact half-width, Δn the gap between the surfaces and $E*(t)$ the time-dependent equivalent elastic modulus.

studying numerically the retraction of a rigid cylindrical indenter from a viscoelastic half-space for a generic retraction velocity. In this manner, we can relax the assumptions made in analytical models, i.e., that the system is close to the JKR-limit, that the viscoelastic effects are confined near the peeling edge or that the peeling edge behaves as a sharp crack opening with a constant velocity in mode I. Hence, we can test the validity of these hypotheses. In particular, although the simulations show a significant adhesion enhancement due to viscoelasticity, we find that the instantaneous limit is not reached unless the retraction velocity and the Maugis parameter are very high. Moreover, we provide a parameter that allows estimating when viscoelasticity can cause significant hysteresis in the presence of adhesion. This parameter can be helpful for experimentalists in judging whether viscoelasticity is relevant in their experiments.

The numerical results are obtained using the Green's function method presented by Van Dokkum and Nicola [23]. It is based on a boundary element method, which allows for meshing the surface only. The quasi-static solution of the equation of motion is obtained numerically in Fourier space, where the coupling between surface displacements and tractions is non-local. A similar method was also presented by Carbone and Putignano [24], who studied the steady-state sliding of a ball through a viscoelastic substrate and showed contact asymmetry caused by viscoelasticity. This method, although more computationally efficient than ours, can only consider steady-state conditions and hence is not suitable for the present study. A method very similar to ours was also presented by Bugnicourt et al. [25], who use the model to study the loading of viscoelastic rough surfaces.

2. Problem definition

In this work, we consider the contact mechanical problem of a rigid and macroscopically smooth frictionless indenter retracting from a viscoelastic isothermal half-space with an adhesive interface. The indenter is an infinitely long cylinder, and the problem is solved in the xz-plane, under plane strain conditions. The height of the cylinder, with radius R, is represented by the common parabolic approximation,

$$h(x) \equiv \frac{R}{2}\left(\frac{x}{R}\right)^2, \tag{1}$$

where x is the distance from the vertical axis of symmetry. Fig. 1 provides a schematic representation of the contact mechanical problem considered in this work. In order to obtain the initial conditions, the substrate is first loaded to a maximum indentation depth h_0. The corresponding adhesive contact problem is solved under the assumption that the substrate behaves elastically (with the relaxed modulus). Note that in this way, we can replicate the initial conditions that would be obtained if the viscoelastic substrate would first be loaded to the same depth and then left to relax for a long period of time. From this point, the indenter is retracted at a constant velocity v_z, and the effects of viscoelasticity are studied. Isothermal conditions are assumed during the whole process. The substrate is assumed to be linear elastic and incompressible in dilatation and viscoelastic in shear. For simplicity, we have described the viscoelastic material as a standard linear solid (also known as Zener model) [26], although different models can be straightforwardly implemented, if required. Accordingly, we can express shear deformation through the relaxation function

$$\mu(t) \equiv \mu_0 + (\mu_\infty - \mu_0)e^{-t/\tau}, \tag{2}$$

where τ is the relaxation time and μ_0 and μ_∞ are the two coefficients used to define the standard linear solid. In contact problems, it is often convenient to define the equivalent elastic modulus as $E*(t) = 2\mu(t)/(1-\nu)$, where ν is the Poisson's ratio, here taken to be 0.5. From (2), the equivalent elastic modulus reads

$$E*(t) \equiv E*_0 + (E*_\infty - E*_0)e^{-t/\tau} = E_0 * \left(1 - \left(1 - \frac{1}{k}\right)e^{-t/\tau}\right), \tag{3}$$

where $E^*_\infty \equiv E^*(t \to 0)$ is the equivalent elastic modulus in the instantaneous limit (which characterizes the elastic response when the deformation rate $\dot{u}\to\infty$), $E^*_0 \equiv E^*(t \to \infty)$ is the equivalent elastic modulus in the relaxed limit (which characterizes elastic response when $\dot{u}\to 0$) and $k = E^*_0/E^*_\infty$. Throughout the paper, E^*_0 will be used as a reference. Note that there are other works, like [19], where E^*_0 is used to denote the modulus in the instantaneous limit and E^*_∞ in the relaxed one.

Adhesion is described following the Dugdale-Maugis model [27,28], i.e., the attractive part of the traction is given by $\sigma_a = \Delta\gamma_0/\Delta_{max}$, where $\Delta\gamma_0$ is work of adhesion, and Δ_{max} is the maximum separation at which adhesive tractions are active, i.e., the interaction length. Over-closure is prevented by adding a hard-wall constrain, so that the surface is under the following conditions:

$$\begin{array}{l} g(x,t) = 0, p(x,t) < \sigma_a, \text{intimate contact;} \\ 0 < g(x,t) \le \Delta_{max}, p(x,t) = \sigma_a, \text{adhesive } zone; \\ g(x,t) > \Delta_{max}, p(x,t) = 0, \text{out of contact.} \end{array} \tag{4}$$

where $g(x,t) = h(x) + u_z(t) - u(x,t)$ is the gap between the two bodies, $u(x,t)$ is the normal displacement of the viscoelastic solid and $u_z(t)$ the displacement of the rigid indenter and $p(x, t)$ indicates the (normal) stresses at the interface (defined as positive when attractive).

3. Theoretical background

Before presenting the numerical method, let us revisit a few interesting analytical results from the literature that will help in discussing the results of the numerical model. First, we introduce the effective work of adhesion for opening cracks, a problem that can be directly related to our retraction problem. Then, we present the load-area response in the two limits of high and low retraction rate.

3.1. Effective work-of-adhesion

The hysteresis in the load-to-area curve has been identified as caused by a mechanism acting near or at the interface and can thus be described by a change in the effective work of adhesion $\Delta\gamma_{eff}$. The peeling edges of the contact during retraction of the indenter can be described as cracks opening in mode I. Following Persson and Brener [20], and Carbone and Persson [21], the flow of energy into the crack-tip needed to advance the crack is

$$\dot{\rho}G(\dot{\rho}) = \dot{\rho}G_0 + P(\dot{\rho}), \tag{5}$$

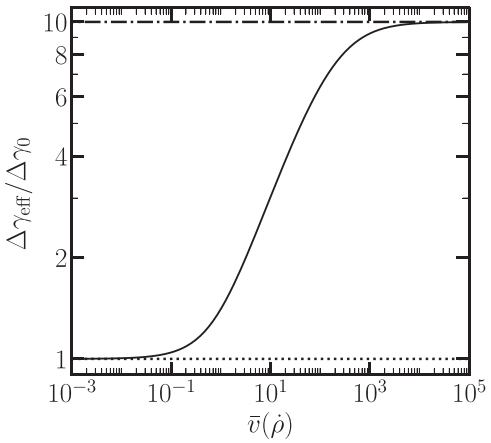

Fig. 2. The normalized effective work of adhesion $\Delta\gamma_{\rm eff}/\Delta\gamma_0$ depicted as a function of the normalized velocity $\bar{v}(\dot{\rho})$ with $E^*_\infty/E^*_0 = 10$, as computed using (8).

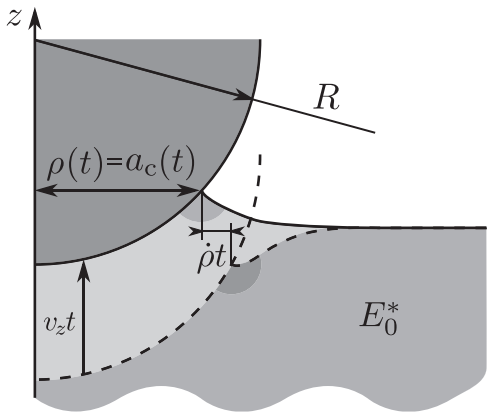

Fig. 3. Schematic representation of the retraction of the smooth frictionless rigid cylindrical indenter from the viscoelastic adhesive solid. The dashed lines represent the original configuration before the retraction of the indenter. The region in which viscoelastic effects are relevant is indicated by darker shaded regions.

where ρ indicates the position of the crack-tip, $\dot{\rho}$ its velocity, $G(\dot{\rho})$ is the energy needed to advance the crack by unit area, G_0 the crack propagation energy per unit area in the absence of viscoelasticity and $P(\dot{\rho})$ is the energy dissipation per unit length of created crack line and per unit time. Now, following LEFM theory, one defines $G_0 = \Delta\gamma_0$. Similarly, for a viscoelastic material, the relation $G(\dot{\rho}) = \Delta\gamma_{\rm eff}(\dot{\rho})$ is used to define the effective work of adhesion. Following Persson and Brener [20], and Carbone and Persson [21], one can assume that: (1) the radial velocity $\dot{\rho}$ is constant; (2) viscous dissipation is confined to a region near the peeling edges, so that far from it, the response is purely elastic with effective modulus E^*_0; (3), adhesion is short-ranged; and (4), the stress field is translational invariant and moves at a constant velocity $\dot{\rho}$. The crack-tip has a certain radius $c(\dot{\rho})$, which is a priori unknown. Under these assumptions one can compute the viscous dissipation and then, using (5), the effective work of adhesion as [20].

$$\frac{\Delta\gamma_{eff}(\dot{\rho})}{\Delta\gamma_0} = \left(1 - \frac{2}{\pi}E*_0 \int_0^1 \frac{\sqrt{1-\overline{\omega}^2}}{\overline{\omega}} Im\left(\frac{1}{\widetilde{E}*\left(\frac{2\pi\dot{\rho}\overline{\omega}}{c(\dot{\rho})}\right)}\right) d\overline{\omega}\right)^{-1}, \tag{6}$$

where $\widetilde{E}(\omega)$ represents the elastic modulus in the frequency domain (i.e., the Fourier transform of (3)), $\overline{\omega} \equiv \omega/\omega_c$ is the frequency normalized by the critical frequency $\omega_c = 2\pi\dot{\rho}/c(\varrho)$ and $\mathrm{Im}(\bullet)$ the imaginary part of the complex number $\bullet$. Following Persson and Brener [20], the crack-tip radius $c(\dot{\rho})$ can be related to the effective work of adhesion by

$$c(\dot{\rho}) = \frac{\Delta\gamma_{\rm eff}(\dot{\rho})E_0*}{\pi\sigma_c^2}, \quad \text{thus} \quad c_0 \equiv c(\dot{\rho}\to 0) = \frac{\Delta\gamma_0 E_0*}{\pi\sigma_c^2}, \tag{7}$$

where σ_c is the fracture stress and c_0 the crack-tip radius in the relaxed limit. Using (6) and (7), one can simultaneously solve for the crack-tip radius and the effective work of adhesion. For the standard linear solid model,

$$c(\dot{\rho}) = \frac{\Delta\gamma\mathrm{eff}}{\Delta\gamma_0} = \left(1 - \left(1 - \frac{E*_0}{E*_\infty}\right)\left(\sqrt{1+\left(\frac{\overline{c}(\dot{\rho})}{v(\dot{\rho})}\right)^2} - \frac{\overline{c}(\dot{\rho})}{\overline{v}(\dot{\rho})}\right)\right)^{-1}, \tag{8}$$

where $\overline{v}(\dot{\rho})$ is the dimensionless velocity and $\overline{c}(\dot{\rho})$ the normalized crack-tip radius given by

$$\overline{v}(\dot{\rho}) \equiv \frac{2\pi\dot{\rho}\tau}{c_0}, \qquad \text{and} \qquad \overline{c}(\dot{\rho}) \equiv \frac{c(\dot{\rho})}{c_0} = \frac{\Delta\gamma\mathrm{eff}(\dot{\rho})}{\Delta\gamma_0}. \tag{9}$$

We note that Persson et al. [20,21] use a finite fracture stress σ_c at the crack-tip which is assumed to be characteristic for the given material. We have replaced the critical fracture stress σ_c with the adhesive traction σa to stress that the interfacial interaction is not a property of the viscoelastic solid. Numerically solving Eq. (8) for $\overline{c}(\dot{\rho})$ gives the normalized effective work of adhesion $\Delta\gamma_{\rm eff}/\Delta\gamma_0$ as a function of the normalized velocity $\bar{v}(\dot{\rho})$ with moduli $E^*_\infty/E^*_0 = 10$ in Fig. 2. Clearly, the effective work of adhesion has two asymptotes. In the limit of a vanishing crack-tip velocity, the effective work of adhesion is $\lim_{\dot{\rho}\to 0}\Delta\gamma_{\rm eff}/\Delta\gamma_0 = 1$, whereas in the limit of an infinitely large velocity, $\lim_{\dot{\rho}\to\infty}\Delta\gamma_{\rm eff}/\Delta\gamma_0 = E_\infty * /\mathrm{E}*_0$. These two limiting cases are considered next.

3.2. The load to area response in the two elastic limits

Fig. 3 presents a schematic of the retraction problem studied in this work. It can be viewed as two Mode I cracks advancing with velocity $\dot{\rho}(t) = -\partial a_c/\partial t$. In the previous section, a relation between the work of adhesion and the crack-tip velocity $\dot{\rho}$ was given. However, this velocity is a priori unknown but controlled by the retraction velocity v_z. Hence, load-to-area curves cannot be directly obtained from (8). In this section, we present such curves for the two limiting behaviours at high and low retraction rates. For this we assume again that viscoelastic dissipation is only present in a small region around the peeling edges.

Under these assumptions, the response in both limits follows that of a purely elastic material. Hence, we start by reviewing the response of an elastic substrate. In this case, the contact response is characterised by the Maugis parameter $\lambda \equiv \left(\Delta\gamma^2 R/\left(E*^2\Delta^3_{\max}\right)\right)^{\frac{1}{3}}$, which was originally introduced by Maugis (see, e.g., [28]) for the ball-on-flat contact and later shown to be relevant also in the cylinder-on-flat contact [29]. The Maugis parameter is large for contacts that behave according to JKR theory [16], and small for contacts that follow DMT theory [30]. JKR-type adhesion is typically encountered when studying the contact of a rigid ball with a relaxed substrate, due to the large radius and small elastic modulus. It is characterized by a vanishing interaction length, $\Delta_{\max} \simeq 0$, and a very small adhesive annulus. According to [29], the load-area relation for $\lambda > 3$ already coincides with the JKR-response. The two-dimensional JKR solution gives a relation between the dimensionless total load L_n and contact half-width a_c as

$$\frac{\pi^{-3/2}}{4}\overline{a}^2 = \frac{\overline{L_n}}{\sqrt{\overline{a_c}}} + \sqrt{2\pi}, \tag{10}$$

where the load and the contact half-width are normalized as

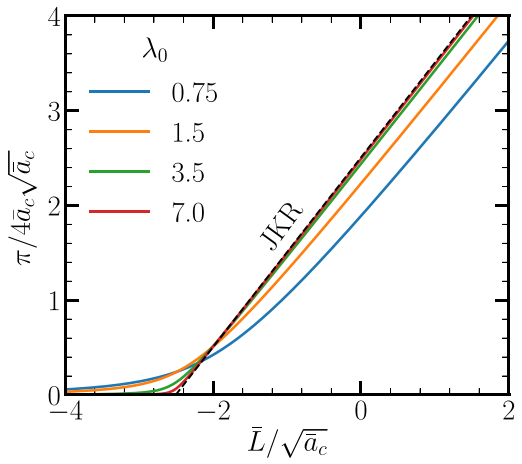

Fig. 4. The scaled contact half-width $(\pi/4)\bar{a}_c\sqrt{\bar{a}_c}$ as a function of the scaled pressure $\bar{L}_n/\sqrt{\bar{a}_c}$, as computed using Eqs. (12) and (13). Elastic conditions are assumed. The dashed black line corresponds to the JKR-limit following Eq. (10).

$$\bar{a}_c \equiv \frac{a_c}{\sqrt[3]{\frac{\Delta\gamma R^2}{E^*}}}; \qquad \text{and} \qquad \bar{L}_n \equiv \frac{L_n}{\sqrt[3]{R\Delta\gamma^2 E^*}}. \tag{11}$$

In cases where λ is below 3, the behaviour of the system departs from the JKR-solution. A more complex relation, valid for the whole range of λ, was given by Baney and Hui [8] as

$$\bar{L}_n = \frac{\pi}{4}\bar{a}_c^{-2} - 2\lambda\bar{a}_c\sqrt{m^2-1}, \tag{12}$$

where $m \equiv a_a/a_c$. Note that the total half-width aa includes the intimate contact and the adhesive region. Eq. (12) is numerically solved together with

$$\lambda\bar{a}_c^2\frac{1}{2}\left(m\sqrt{m^2-1} - \operatorname{arccosh}(m)\right) + \lambda^2\bar{a}_c\frac{4}{\pi}\left(\sqrt{m^2-1}\operatorname{arccosh}(m) - m\log(m)\right) = 1. \tag{13}$$

As $\lambda \to \infty$, (12) turns into the two-dimensional JKR solution given by (11) (usually $\lambda > 3$ is sufficient). As a reference, Fig. 4 shows the scaled load-to-contact half-width for different λ. By virtue of the scaling and the choice of axes, the JKR-solution is given by a straight line with slope 1 and the intercept with the vertical axis at $\sqrt{2\pi}$. For $\lambda \geq 3.5$ the agreement with JKR-solution is excellent but becomes poorer for smaller values of λ. It should be noted that the deviation from the elastic JKR curve, for small values of λ, mostly consists of a horizontal translation and a slight change of slope. Only towards complete withdrawal of the indenter a large discrepancy is observed with respect to the JKR-solution, with a larger tensile load reached before full separation of the bodies. This region is, however, only achievable under separation controlled retraction. It is important to stress that, when the work of adhesion is not known a priori, the horizontal translation and the rotation are not identifiable. Hence, it would be easy to erroneously identify even the case $\lambda = 0.75$ as following closely the JKR solution.

In the relaxed limit, which corresponds to $v_z \to 0$ and $\dot{\rho}\to 0$, the retraction is done slowly enough so that the material does not show viscoelasticity. Hence, the previous discussion holds by simply substituting E^* by E^*_0 and $\Delta\gamma$ by $\Delta\gamma_0$. In this case, we can define a relaxed Maugis parameter as $\lambda_0 \equiv \left(\Delta\gamma_0^2 R/\left({E_0^*}^2\Delta_{\max}^3\right)\right)^{\frac{1}{3}}$ When $v_z \to \infty$, thus $\dot{\rho}\to\infty$, one finds, instead, the instantaneous limit. In this limit, and according to (8), the work of adhesion can be seen as constant and given by $\Delta\gamma_\infty \equiv \Delta\gamma_0 E^*_\infty/E^*_0$. Since we assume that viscoelastic effects are concentrated near the edge of the contact, the bulk is still characterized by the relaxed elastic modulus E^*_0. Hence, one recovers again an elastic behaviour, with $E^* = E^*_0$, albeit with a larger work of adhesion corresponding to the instantaneous state of the interface and a Maugis parameter specific to the instantaneous limit, i.e., $\lambda_\infty \equiv \left(\Delta\gamma_0^2 R/\left((E^*_\infty)^2\Delta_{\max}^3\right)\right)^{\frac{1}{3}}$. In a general situation, due to the increase in work of adhesion, the effective Maugis parameter becomes smaller than λ_0 and larger than λ_∞. This is why viscoelastic effects result also in a departure from the JKR-limit, as can be seen by contrasting the curves in Fig. 4. This is further assessed in the following section.

We here note that Greenwood and Johnson [19] indicated that, since the pressure spike at the peeling edge caused by adhesion is infinite under JKR-theory, the stress and strain rates would also be infinite for any finite velocity. Therefore, any viscous material around the peeling edge would always be in the instantaneous limit. They noted that this was against observations and therefore, suggested to use a more realistic description of the crack tip (e.g., the Barenblatt crack), which accounts for the fact that the stress peak at the peeling edges is not infinitely high and that adhesion acts over a finite, although small, distance. To our knowledge, this approach has never successfully been applied to describe the unloading of a cylinder from a flat. In our numerical model, where adhesion acts over a small distance $\Delta_{\max}$, the instantaneous limit is not reached even for high values of λ_∞, and the model is therefore appropriate to study the retraction of an indenter from a viscoelastic material.

4. Numerical method: solution through Green's function Molecular Dynamics

The numerical simulations are performed using the Green's Molecular Dynamics (GFMD) technique for viscoelastic solids presented by Van Dokkum and Nicola [23]. The surface of the viscoelastic substrate is discretized with n_x equi-spaced grid points on which the externally applied load rate is prescribed in real space. Tractions and displacements are computed in Fourier space. Following [23], a relation between tractions and displacements at the surface for a given wavenumber q, at time t, can be established as

$$p(q,t) + \tau\dot{p}(q,t) = -8|q|(E^*_0 u(q,t) + \tau E^*_\infty \dot{u}(q,t)) \tag{14}$$

Note that, in (14), p and u are expressed in Fourier space. To obtain (14), one first solves, in Fourier space, the elastic problem of sinusoidal traction causing sinusoidal deformation. The result is then translated to the viscoelastic case using the correspondence principle. Finally, (3) is used to particularize the solution to the case of a standard linear solid to obtain (14). The reader is directed to [23] for a detailed derivation. The exact numerical integral solution requires the storage of the whole history of stresses and displacements. It therefore becomes, with time, progressively more demanding in terms of memory and computational time. Hence, we opt for integrating Eq. (14) over time-step Δt using the semi-analytical method proposed in [23]. The quasi-static solution at time $t_n + \Delta t$, with the total simulation time t_{total} divided into n equal time periods Δt, is obtained by solving the equation of motion for each mode with a unit mass in reciprocal space over a dimensionless time step Δt^* via the position (Störmer-)Verlet algorithm [31]. The maximum time step $\Delta t_{\max} \equiv \tau E^*_1/E^*_\infty$ [25]. Note that the dimensionless time t^* is a numerical operator without any physical meaning while Δt has the dimension of time. Since in Fourier space the displacement modes decouple, each mode can be damped independently which leads to a fast converging solution. The solution is found quickest by critically damping each mode. We use the relaxed critical damping coefficient which is described by a non-monotonous equation:

$$c_{cr} = 2\sqrt{8|q|E^*_0} - 8|q|E^*_0\Delta t^*, \tag{15}$$

to ensure that the solution is always underdamped. In this way, we achieve the correct solution, albeit not in the fastest manner.

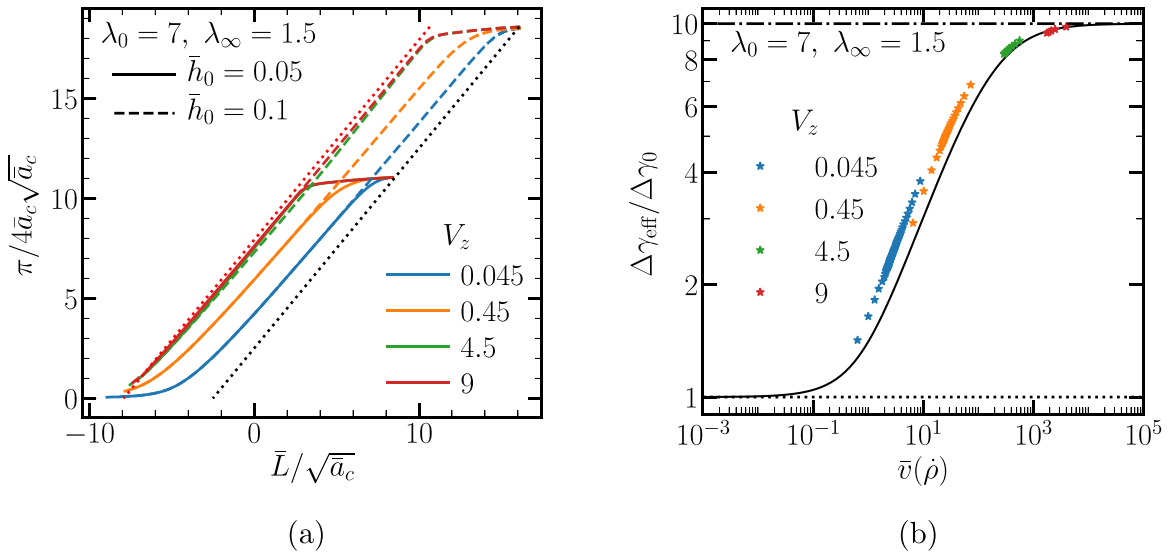

Fig. 5. (a) The scaled contact area versus load for $\{\lambda_0, \lambda_\infty\} = \{7, 1.5\}$, various normalized velocities and two indentation depths. The black dotted line indicates the relaxed limit while the red dotted line indicates the instantaneous limit. (b) The normalized work of adhesion $\Delta\gamma_{\text{eff}}/\Delta\gamma_0$ as a function of the dimensionless radial velocity $\bar{v}(\dot{\rho})$ for the cases shown in (a). The solid black line indicates the theoretical prediction (8) by Persson et al. [20,21]. (For interpretation of the references to colour in this figure legend, the reader is referred to the web version of this article.)

When the a priori calculated dimensionless equilibrium time $t_{\text{equil}}{}^*$ is reached, the stresses and displacements in reciprocal space are saved as input for the next dimensional time-step. The attractive and repulsive tractions are calculated in real space, where the hardwall condition returns the coordinates of the surface nodes to the rigid body in case of over-closure. Non-adhesive contact simulations for viscoelastic bodies were validated in [23]. The pseudo-code used to obtain the numerical results is presented in Appendix A.

We note that the relation between p and u, given in (14), degenerates when $q = 0$, which corresponds to the mean values of the pressures and deformations. The mean value of the deformation must be zero, since the body is incompressible and periodic: volume must be conserved and the only surface that can displace is the contact one. Periodicity allows us to define a finite mean separation, differently from the case of a non-periodic 2D body, where the mean deformation is undefined (see e.g., [32]). However, this quantity is somewhat arbitrary, since it depends on the width of the periodic cell. Hence, we will not show any result using the approach. Nonetheless, this definition does allow us to define a meaningful retraction velocity.

4.1. Choice of parameters

The viscoelastic substrate is modelled as a semi-infinite unit cell, periodic in x-direction. The ratio between the radius of the indenter and the size of the periodic unit cell is taken to be $\Delta L/\mathrm{R} = 10$, to ensure no interaction between neighbouring periodic intenders at the maximum indentation depth, $\bar{h} \equiv h_0/\mathrm{R} = 0.1$. The indentation depth is taken to be sufficiently small, to warrant the deformation is in the small-strain regime. The substrate is characterized by the effective moduli, such that $k = E^*{}_0/E^*{}_\infty = 0.1$. The relaxed Maugis parameter and the retraction velocities will be varied.

The rigid indenter displaces as follows:

$$u_z(t) \equiv \left\{ \begin{array}{lll} -h_0, & \text{for} & t < 0; \\ v_z t - h_0, & \text{for} & t \geq \tau, \end{array} \right\} \tag{16}$$

where v_z is the retraction velocity, i.e., the rate at which the mean separation between the indenter and the substrate increases, and u_z is the penetration of the indenter with respect to the undeformed substrate. Following the dimensional analysis in Appendix C, the non-dimensional retraction velocity is defined as

$$V_z = v_z \tau (E*{}_0{}^2/\Delta\gamma_0{}^2 R)^{1/3}, \tag{17}$$

and we take the values $V_z = 0.045$, 0.45, 4.55 and p. Two different indentation depths, $\bar{h}_0 = 0.1$ and 0.05, are considered to verify that the response is independent of the initial conditions, except for a given initial transient response. At times $t < 0$ an indention is performed with effective elastic modulus $E^* = E^*{}_0$. The deformed surface at maximum indentation depth is obtained by solving the adhesive contact problem over a single time-step Δt imposing that the substrate behaves elastically. This is equivalent, but much faster than indenting very slowly a viscoelastic substrate or letting the substrate relax post-indentation. The total simulation time t_{total} is chosen to achieve complete detachment. As demonstrated in Appendix B, convergence of the results is ensured by using a spatial discretization $n_x = 2^{17}$ and a temporal discretization $\Delta t/\Delta t_{\text{max}} = 50$.

5. Results

It is important to note that, unlike the analytical models previously presented, our numerical model does neither assume that the system is in the JKR-limit, nor that the viscoelastic effects are confined to the contact edges, nor that the peeling edge should behave as a sharp crack opening in mode I with constant velocity. This allows us to test the validity of the aforementioned assumptions. Even so, we select relaxed Maugis parameters large enough ($\lambda_0 > 3$) so that the elastic response is within the range in which JKR-theory is applicable, and any deviation from this theory is due to viscoelastic effects only.

5.1. The effect of the retraction velocity

In Fig. 5a, we show the contact area as a function of the scaled load for a viscoelastic substrate with Maugis parameters $\{\lambda_0, \lambda_\infty\} = \{7, 1.5\}$. The indenter is retracted from an indentation depth $\bar{h}_0 = 0.1$ (dashed line) and $\bar{h}_0 = 0.05$ (solid line). The relaxed and instantaneous limits, defined in the previous section, are indicated by a black dotted and a red dotted line, respectively. Increasing the non-dimensional retraction velocity from 0 to 9 shifts the behaviour of the contact from the relaxed towards the instantaneous limit. As apparent from (17), an increase in the non-dimensional velocity, and therefore a shift towards the

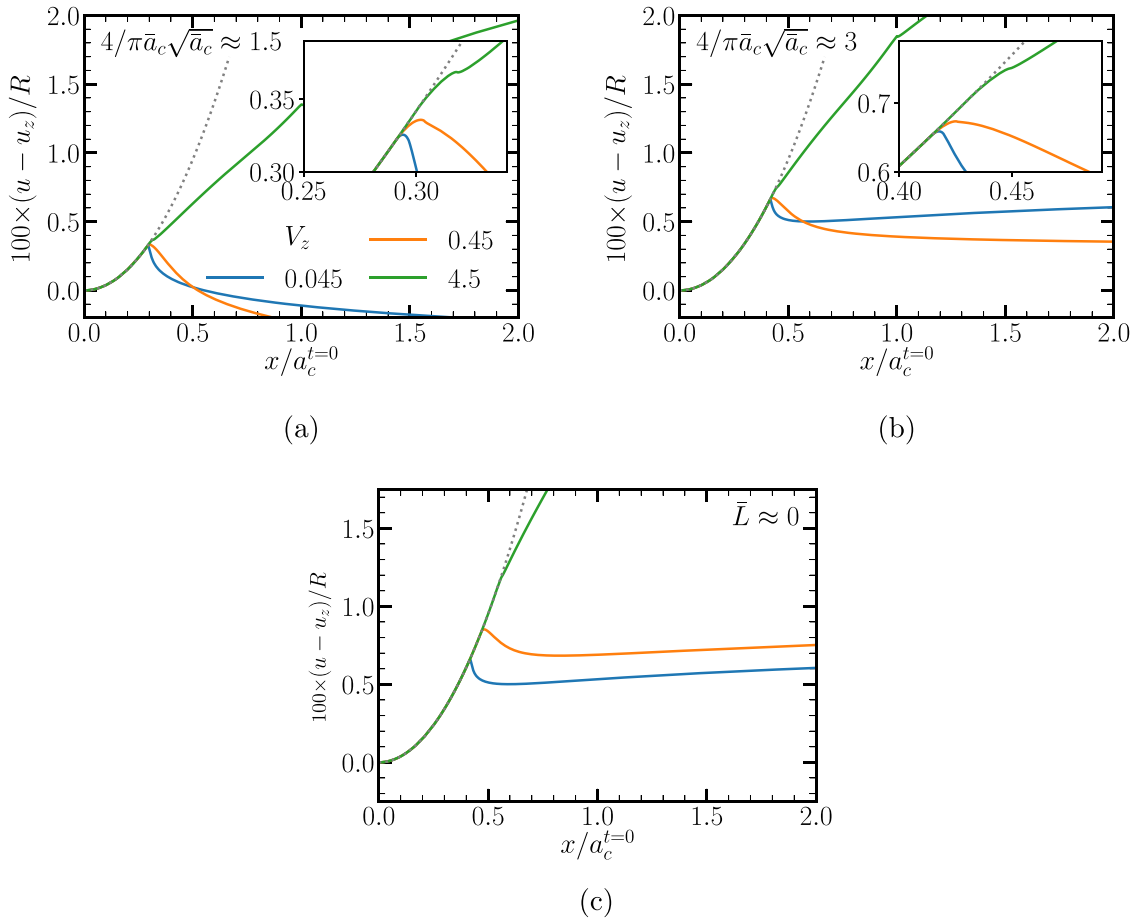

Fig. 6. Scaled surface shape as a function of the position in x-direction, which is normalized by the initial contact area $a_c^{t=0}$. The results are shown for $\{\lambda_0, \lambda_\infty\} = \{7, 1.5\}$ at two values of $\bar{a}_c$ or at $\bar{L} = 0$, as indicated in each sub-figure. The insert in Fig. 6a and b show a zoom in of the surfaces shapes near the contact edge.

instantaneous limit, can be achieved by either an increase of velocity or by a decrease of radius or the relaxation time of the viscous material.

The initial indentation depth only affects the initial stages of retraction, when the velocity of the peeling edge changes from zero to a finite value. After that, a 'steady-state' is reached where the initial conditions do not matter any more. Only in the case of the highest V_z, does it take longer for the curves to superimpose. This is in agreement with the experimental observation that the initial conditions only affect the pull-off force when roughness is prevalent [33]. Towards the end of unloading, curves at low velocities present a tail, similar to that shown in Fig. 4 for low Maugis parameters. Unlike in that case, however, this is not caused by a departure from the JKR-limit. Instead, the contact area is small enough for the two edges to interact, which leads to an acceleration of the peeling edges and to an increase in the effective work of adhesion. At high velocities, instead, an unstable jump occurs at a relatively high a_c. Note that the normalization does not permit plotting states with $a_c = 0$ and hence we have only plotted the curves at the smallest stable contact state.

It should be noted that the JKR theory does not apply in the initial transient period and just before the detachment of the indenter. Since a similar transient response is to be expected also in experimental studies, it is important, when fitting experimental data, to exclude the data obtained at the onset and at the end of retraction. For instance, Tiwari et al. [13] studied experimentally the indentation and retraction of a rigid sphere on a viscoelastic substrate and showed that the JKR solution could represent adequately the load area relation during retraction except at the onset of retraction. Presumably, the agreement with the JKR-solution would have been even better if the transient was explicitly recognized and the data points at the beginning of retraction were excluded. In this sense, plotting the experimental load-area data with the same scaling as in Fig. 5a can help in identifying the data that deviates from the JKR-solution and should be disregarded.

In Fig. 5b, the work of adhesion is shown as a function of the non-dimensional peeling edge velocity, $\bar{v}(\dot{\rho})$. When computing the work of adhesion, it must realized that the curves in Fig. 5a, are not straight lines. This is true even under 'steady state' conditions, where the change in peeling-edge velocity leads to a change in work of adhesion. Hence, using a linear fit to assign a unique value for the work of adhesion to the whole retraction process, as done in several previous works [12,13,21], would lead to a certain arbitrariness in the calculation. Here, instead, we find the normalized effective work of adhesion $\Delta\gamma_{\text{eff}}/\Delta\gamma_0$ as a function of the radial velocity $\dot{\rho}$ for each numerically obtained point in Fig. 5a. For that, a line with unit gradient passing through each point is constructed and the work of adhesion is obtained by taking the intercept of the line with the y-axis. Clearly, an increase in the retraction velocity produces an increase of $\dot{\rho}$ and thus an increase of the effective work of adhesion, in accordance with the theoretical analysis in Section 3. One should also note that each retraction curve exhibits a range of velocities of the peeling edges and correspondingly a range of works of adhesion. Therefore, defining a single value for the work of adhesion to describe the whole retraction process is not accurate, unless the contact satisfies the relaxed or the instantaneous limits, see Section 3, which in practice does not happen. The analytical theory outlined by Persson and collaborators, given by Eq. (8) is also represented. As it can be seen, the numerical results align quite well with this equation, which was derived to model the opening of cracks in mode I. This indicates that, for the cases considered here, which are close to the JKR-limit, it is appropriate to assume that the contact behaves as two isolated cracks opening in

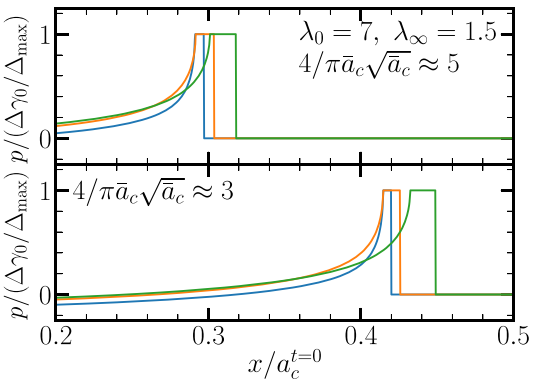

Fig. 7. Surface pressure as a function of the position in x-direction, which is normalized by the initial contact area $a_c^{t=0}$. The results are shown for $\{\lambda_0, \lambda_\infty\} = \{7, 1.5\}$ at two values of $\bar{a}c$ or at $\bar{L} = 0$, as indicated.

mode I, and also that the viscoelastic effects are confined to a small region around the edges of the contact. We note that perfect agreement should not be expected, as some assumptions made in the analytical models do not hold exactly. For instance, the peeling velocity is clearly not constant, specially during the transient observed at the onset of retraction.

Fig. 6 a shows the surface shape $(u - u_z)/R$ as a function of the normalized radius $\rho/a_c^{t=0}$ for the relative contact areas $4/\pi\ \bar{a}_c^{-3/2} = 5$ and 3. Fig. 6b shows a closer look of the same cases around the contact edge. An increase in the retraction velocity leads to a smaller separation between the surfaces that used to be in contact since the body has less time to recover. Hence, the contact area under adhesion becomes larger and the peeling angles more acute. As indicated in [19], this change is characteristic of a departure from the JKR-limit. Another way to understand this transition is to realize that the increased viscous dissipation must be compensated by an increase of work of adhesion, as also shown in Fig. 5b. This increase also results in a reduction of the effective Maugis parameter, which will lay between λ_∞ and λ_0 (note that $\lambda_\infty < \lambda_0$). Owing to the reduction of the Maugis parameter, the departure from the JKR-limit as the instantaneous limit is approached is not surprising. We note, however, that all cases are nonetheless fairly close to the JKR-limit, as seen in Fig. 5a. Moreover, this departure is not easily seen by looking solely at the load-to-area curves. Probably, these departures would be more obvious for larger E_∞/E_0, where λ_∞ would be much smaller.

The reader will notice that some lines cross in Fig. 6a. This is solely caused because the profiles are shown at constant contact area, which however corresponds to different applied loads. In Fig. 6c it is shown that, when the load is the same, the lines do not cross. As expected, a smaller velocity leads to a larger relaxation of the viscoelastic solid and thus to a larger separation between the two surfaces.

Fig. 7 shows the pressure distribution around the contact edge, which corresponds to Fig. 6a and c. Clearly, the width of the adhesive annulus increases with retraction velocity. A larger velocity leads to a more instantaneous behaviour and therefore approaches closer the instantaneous Maugis parameter $\lambda_\infty = 1.5$. As discussed in Section 3, a smaller Maugis parameter is characterized by a larger adhesive annulus. Although the increase in adhesive area is small, since the adhesive pressures are large compared to the repulsive ones, this is sufficient to change the overall behaviour.

5.2. The effect of the Maugis parameter

In the previous section we saw how viscoelastic effects can reduce the effective Maugis parameter, making the contact depart from the JKR-limit. In this section we will show that the value of the relaxed Maugis parameter λ_0, i.e., how close the elastic simulations is to the JKR-limit influences the viscoelastic response. In Fig. 8a, the contact area is presented as a function of the load for three sets of Maugis parameters $\{\lambda_0, \lambda_\infty\} = \{14, 3\}$, $\{7, 1.5\}$ and $\{3.5, 0.75\}$. The retraction velocity is set to $V_z = 0.9$. Again, the relaxed and instantaneous limits, corresponding to the case $\{\lambda_0, \lambda_\infty\} = \{7, 1.5\}$, are shown as a reference. It is apparent in Fig. 8a that an increase of λ_0 renders the system closer to the instantaneous limit. Note that, when λ_0 is increased, the adhesive component of the pressure forms a higher and narrower spike at the contact edges, which induces larger the stress rates at the peeling edge. However, one should notice that while $\lambda_0 > 3$ is sufficient for an elastic contact to converge to the JKR limit in terms of the area-load curve, a much larger λ_0 is needed to reach the instantaneous limit. For instance, when $V_z = 0.9$, we find that $\lambda_0 = 14$ is not sufficient to reach the instantaneous limit. This is because the spike is not sufficiently high and narrow to induce the high stress rates needed to reach the instantaneous limit. Note also that, as the instantaneous limit is approached, the effective Maugis parameter is reduced towards λ_∞. This also contributes towards

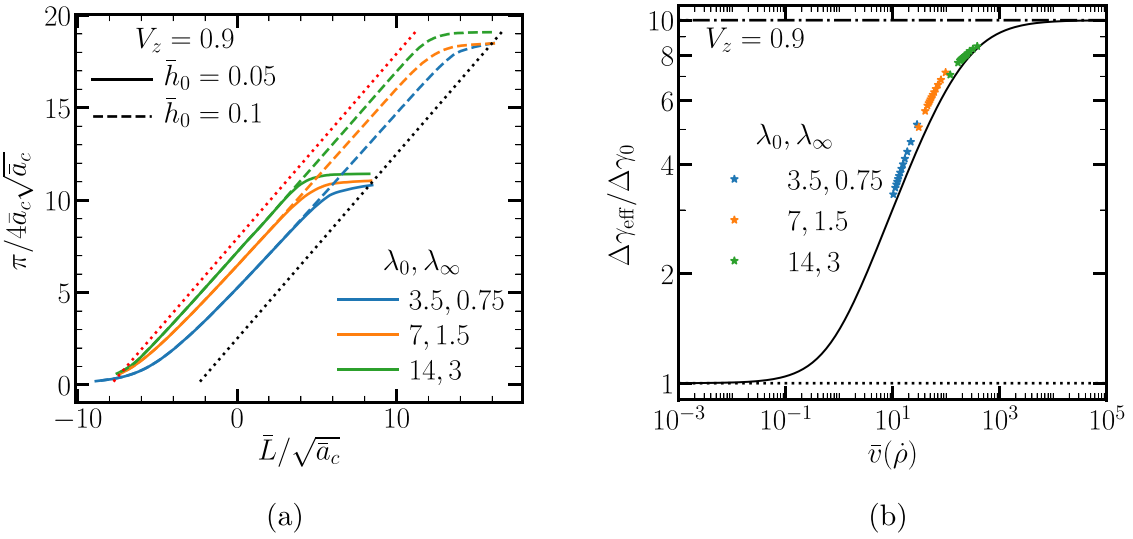

Fig. 8. (a) The scaled contact area vs. load for $V_z = 0.9$, various Maugis parameters and two indentation depths. The black dotted line indicates the relaxed limit while the red dotted line indicates the instantaneous limit. (b) The normalized work of adhesion $\Delta\gamma_{\text{eff}}/\Delta\gamma_0$ as a function of the dimensionless radial velocity $\bar{v}(\dot{\rho})$ for the cases shown in (a). The solid black line indicates the theoretical prediction (8) by Persson et al. [20,21]. (For interpretation of the references to colour in this figure legend, the reader is referred to the web version of this article.)

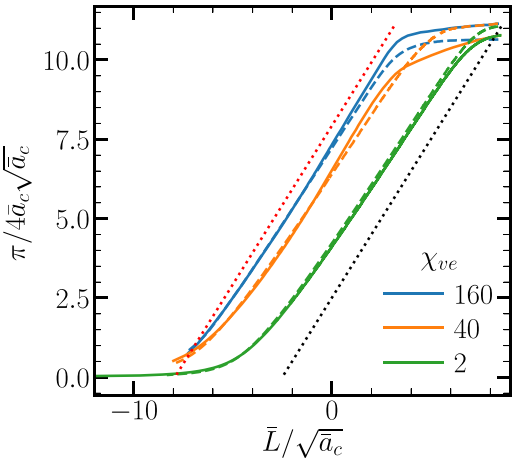

Fig. 9. The scaled contact area vs. load with $\bar{h} = 0.05$ and various combinations of V_z and λ_0. The colours indicate the value of χ_{ve} as indicated in the lower legend. The lines correspond to the pair of values $\{V_z, \lambda_0, \chi_{ve}\} = \{3.6, 7, 160\}$ (blue, solid), {0.9, 14, 160} (blue, dashed), {3.6, 3.5, 40} (orange, solid), {0.9, 7, 40} (orange, dashed), {0.18, 3.5, 2} (green, solid) and {0.045, 7, 2} (green, dashed). The black dotted line indicates the relaxed limit while the red dotted line indicates the instantaneous limit. (For interpretation of the references to colour in this figure legend, the reader is referred to the web version of this article.)

making it harder to reach the instantaneous limit.

The work of adhesion is shown in Fig. 8b, where it is evident that the larger the Maugis parameter, the larger the effective work of adhesion. As in Fig. 5b, the work of adhesion is in general well represented by (8).

5.3. A parameter to estimate the relevance of viscoelastic effects

As discussed in the introduction, several mechanisms have been proposed for adhesion hysteresis. Viscoelasticity has been shown experimentally to be very relevant in some cases [13] but irrelevant in others [15]. We here propose a parameter that can be used to estimate when viscoelasticity is relevant.

We first take note that both increasing V_z and increasing λ_0 lead to a similar effect. This can be rationalized if one assumes that viscoelastic effects are confined to the peeling edge. In order to determine how close the viscoelastic modulus is to the instantaneous one, we estimate the stress rate close to the peeling edge, i.e. the speed with which the adhesive pressure spike moves. An increase in V_z leads to an increase of the peeling edge velocity and hence the pressure spike moves faster and produces higher stress rates. Similarly, an increase in λ_0 makes the spike taller and narrower, also leading to higher stresses rates. In order to attain a quantitative estimation, we simplify the picture by assuming that the spike is the only source of stress. The spike has a width w, reaches a maximum pressure σa and moves with the velocity of the peeling edge. The velocity of the peeling edge can be expressed as

$$\dot{\rho} = \frac{da_c}{du_z}\frac{du_z}{dt} = \frac{da}{du_z}\mathrm{v}_z \tag{18}$$

and hence scales with the retraction velocity v_z. Therefore, we can write

$$\dot{p} \approx \frac{v_z \sigma \mathrm{a}}{w}, \tag{19}$$

where we have ignored the scaling factor given by dac/duz. The width is computed in Appendix D as

$$w = \frac{\pi E^* \Delta_{\max}}{4\sigma_a}. \tag{20}$$

The non-dimensional pressure derivative is given by

$$\dot{P} \approx \frac{V_z}{W} = \frac{4}{\pi}\frac{v_z \tau}{\Delta_{\max}}\lambda_0, \tag{21}$$

where $W = \pi/4/\lambda_0^2$ is the non-dimensional width. Therefore, we can see that the stress rate should approximately scale with a parameter χ_{ve}

$$\chi_{ve} = \frac{v_z \tau \lambda_0}{\Delta_{\max}} = \frac{v_z \tau}{\Delta^2{}_{\max}}\left(\frac{R\Delta\gamma_0{}^2}{E_0^{*2}}\right)^{1/3} = \frac{\sigma_a v_z \tau}{\Delta\gamma_0}\left(\frac{R}{E_0^{*2}\,\Delta\gamma_0}\right)^{1/3}. \tag{22}$$

To test the performance of this parameter, Fig. 9 shows cases with varying V_z and λ_0. Cases with equal parameter but different V_z and λ_0 show a very similar response, confirming that χ_{ve} can be used to estimate the relevance of viscoelastic effects when V_z, λ_0 and the interaction length $\Delta_{\max}$, are known.

For small values of χ_{ve} (say $\chi_{ve} < 2$), the system will be close to the relaxed limit and viscoelastic effects can be neglected. Instead, when it is large (say $\chi_{ve} > 160$), the system will be closer to the instantaneous limit and the work of adhesion will be given by $\Delta\gamma_\infty$. Reviewing each component of (22), we can say that, when the velocity and/or λ_0 are large or $\Delta_{\max}$ is small the system approaches the instantaneous limit. This is because the adhesive pressure forms a sharper, faster moving spike. Finally, if τ is larger, we will also be closer to the instantaneous limit because a longer time will be needed to relax to the relaxed conditions.

As an example of the usefulness of this parameter, we may compare several works in the literature. Unfortunately, values for $\Delta_{\max}$ or τ are not available so the best we can do is to assume that their values do not change significantly in the different experiments and, instead of giving numerical values to χ_{ve} look for trends in this parameter. In the experimental work by Dalvi et al. [15], the authors found viscoelastic effects to be negligible. In that case, the ball radius was small ($R \approx 2.5$ mm), as was the retraction velocity ($v_z \approx 60$ μm/s). On the contrary, the elastic modulus was relatively large ($E^*_0 \approx 1$–10 MPa). This combination of parameters corresponds to a fairly small χ_{ve}. In the work by Tiwari et al. [13], instead, strong viscoelastic effects were noticed. In that case, the radius was of the same order ($R \approx 3.3$ mm) but the retraction velocity was larger ($v_z \approx 400$ nm/s) and the elastic modulus was much smaller ($E^*_0 \approx 25$ kPa). Hence the value of χ_{ve} was much larger in that case. Similarly, Baek et al. [14] observed a strong hysteresis at a small velocity ($v_z = \approx 60$ nm/s) and high stiffness (E^*_0 ≈ 2.6 MPa) when studying a system with a large radius ($R \approx 200$ mm), which would also lead to a high χ_{ve} value. All these results are consistent with the behaviour predicted by the parameter defined in (22).

It should be noted that, unfortunately, this parameter is not trivial to be estimated experimentally due to the presence of $\Delta_{\max}$. We note, however, that the Maugis parameter shares the same limitation. Also we have proven the numerical performance of the parameter using the standard linear solid for viscoelasticity. Although we expect the results to be qualitatively similar for various viscoelastic materials, we do note that a single value for τ might not be sufficient to describe materials that deviate significantly from this model. An alternative in this case could be to choose a reference time-scale, as suggested by Persson et al. [34], equal to the inverse of the frequency at which viscous dissipation is maximum.

6. Conclusions

In this paper, we have analysed the retraction of a cylindrical indenter from a viscoelastic substrate. In agreement with analytical theories based on LEFM, we find that the load-to-area relationship lays between two limits, both of which can be characterized using JKR-theory: in the relaxed limit no viscoelastic effects are seen, while in the instantaneous limit there is an increase in the work of adhesion, $\Delta\gamma_\infty = E^*_\infty/E^*_0\Delta\gamma_0$. Increase in the normalized retraction velocity and/or relaxed Maugis parameter enhances the instantaneous behaviour and brings the response closer to the latter limit. We have shown, however,

that a very high velocities and /or a very large relaxed Maugis parameter are needed for the instantaneous limit to be approached.

Differently from the LEFM based theories, the simulations show that a transient period is present at the onset of retraction, in which the contact area reduces only very slowly; and that a tail appears close to the detachment point. Also, we observe a deviation from the JKR-behaviour as the instantaneous limit is approached. Both these features complicate an analysis of the contact based on the JKR-solution. This means that in all practical scenarios, i.e., away from either limit, the area-load curve is translated and rotated with respect to the relaxed limit.

Finally, we have proposed a new parameter,

$$\chi_{ve} = \frac{v_z \tau}{\Delta^2_{max[f_0]}} \left(\frac{R \Delta {\gamma_0}^2}{E_0^{*2}} \right)^{1/3} = \frac{\sigma_a v_z \tau}{\Delta \gamma_0} \left(\frac{R}{E_0^{*2}\, \Delta \gamma_0} \right)^{1/3}, \tag{23}$$

that allows estimating under which conditions viscoelastic effects can be relevant. We find that viscoelasticity can be ignored when $\chi_{ve} < 2$ and that the instantaneous limit is approached when $\chi_{ve} > 160$. This can be particularly useful in experiments where it is unclear whether viscoelasticity contributes to adhesive hysteresis. To show the effectiveness of the parameter, we have shown that the presence or absence of viscoelastic effects in several experimental works in the literature correlates with trends of increasing or decreasing χ_{ve}.

CRediT authorship contribution statement

Jan StevenVan Dokkum: Conceptualization, Methodology, Software, Validation, Formal analysis, Investigation, Writing – original draft, Writing – review & editing, Visualization. **Francesc Pérez-Ráfols:** Conceptualization, Formal analysis, Investigation, Writing – original draft, Visualization. **Leonid Dorogin:** Investigation, Writing – review & editing. **Lucia Nicola:** Conceptualization, Resources, Writing – review & editing, Supervision, Project administration, Funding acquisition.

Declaration of Competing Interest

The authors declare that they have no known competing financial interests or personal relationships that could have appeared to influence the work reported in this paper.

Acknowledgements

This work is funded by the European Research Council (ERC) under the European Union's Horizon 2020 research and innovation programme (grant agreement no. 681813).

Appendix A. Viscoelastic GFMD pseudo-code

(i) Setup rigid indenter with initial surface topography $h(x)_{t_n=0}$;

(ii) Determine damping coefficient vector $c_{cr}(q)$ such that all modes are critically and/or under-damped, and calculate the dimensionless equilibrium time t^*_{equil} for a given dimensionless time-step Δt^*;

(iii) Loop over iteration n with time-step Δt till the time t_{final} is reached. Give the location of the rigid indenter as $z(x)^{indenter}_{t_n+\Delta t} = h(x - \delta^x_{t_n+\Delta t})_{t_n=0} + \delta^z_{t_n+\Delta t}$, where $\delta^z_{t_n+\Delta t}$ and $\delta^x_{t_n+\Delta t}$ are the normal and tangential displacement of the rigid indenter at time $t_n + \Delta t$ respectively.

(a) Loop over Δt^* till the equilibrium time t^*_{equil} is reached.

- Discrete fast Fourier transform (DFFT) surface displacement $u(x)^{new}_{t_n+\Delta t}$ using the FFTW3 library [35].
- Calculate viscoelastic restoring force, $\widetilde{F}(q)^{visco\text{-}elas}_{t_n+\Delta t} \leftarrow \text{Func.}\{\widetilde{u}(q)^{new}_{t_n+\Delta t}, \widetilde{u}(q)_{t_n}, \widetilde{F}(q)_{t_n}, \Delta t\}$;
- Add external force and interfacial force, $\widetilde{F}(q)^{total}_{t_n+\Delta t} \leftarrow \widetilde{F}(q)^{visco\text{-}elas}_{t_n+\Delta t} + \widetilde{F}(q)^{ext}_{t_n+\Delta t} + \widetilde{F}(q)^{if}_{t_n+\Delta t}$;
- Add damping forces, $\widetilde{F}(q)^{total}_{t_n+\Delta t} \leftarrow -\, c_{cr}(q) \frac{\widetilde{u}(q)^{now}_{t_n+\Delta t} - \widetilde{u}^{old}(q)_{t_n+\Delta t}}{\Delta t*}$;
- Use pSV to solve equation of motion, $\widetilde{u}(q)^{new}_{t_n+\Delta t} = 2\widetilde{u}(q)^{now}_{t_n+\Delta t} + \; -\widetilde{u}(q)^{old}_{t_n+\Delta t} + \; + \widetilde{F}(q)^{d}_{t_n+\Delta t}(\Delta t*)^2$
- Assign $\widetilde{u}(q)^{old}_{t_n+\Delta t} \leftarrow \widetilde{u}(q)^{now}_{t_n+\Delta t}$ & $\widetilde{u}(q)^{now}_{t_n+\Delta t} \leftarrow \widetilde{u}(q)^{new}_{t_n+\Delta t}$;
- Reverse DFFT displacement $u(x)^{new}_{t_n+\Delta t}$ into real space, and scale displacement $u(x)^{new}_{t_n+\Delta t}$ with 1/L;
- Implement the hardwall boundary condition, $u(x)^{new}_{t_n+\Delta t} \leftarrow \min\{u(x)^{new}_{t_n+\Delta t}, z(x)^{indenter}_{t_n+\Delta t}\}$;
- Calculate interfacial force $F(x)^{if}_{t_n+\Delta t} \leftarrow \text{Func.}\{u(x)^{new}_{t_n+\Delta t}, z(x)^{indenter}_{t_n+\Delta t}\}$ & DFFT to $\widetilde{F}(q)^{if}_{t_n+\Delta t}$.

(b) DFFT displacement $u(x)^{new}_{t_n+\Delta t}$;

(c) Assign $\widetilde{u}(q)_{t_n} \leftarrow \widetilde{u}(q)^{new}_{t_n+\Delta t}$ & $\widetilde{F}(q)_{t_n} \leftarrow \widetilde{F}^{total}_{t_n+\Delta t}$.

Appendix B. Convergence test

Convergence with increased spatial and temporal discretization is shown here for two cases. The first one, presented in Fig. B1a, corresponds to $V_z = 4.5$ and $\lambda_0 = 7$. Clearly, $n_x = 2^{17}$ and $\Delta t/\Delta t_{max} = 50$ are sufficiently fine to achieve a good spatial and temporal discretization for this case. Note that, with increased λ_0, the pressure spike becomes thinner and hence a finer spatial discretization is needed. Also, with increased retraction velocity, a smaller time step in needed. Hence, the case presented in Fig. B1a demands a discretization finer than any other case considered in this work. Hence, most cases considered in this work will demand a less fine time and spatial grids and can be considered converged as well. Only two cases remain to be checked. The case $V_z = 9$ and $\lambda_0 = 7$ could fail because the higher speed may require a finer temporal discretization. It was tested in a similar fashion (not shown), leading to the conclusion that $\Delta t/\Delta t_{max} = 100$ was needed for convergence to be achieved. It is worth pointing out that a fine time discretization is needed to capture the appropriate pull-off load, as a coarse time discretization leads to an early pull-off. The other case corresponds to $V_z = 0.9$ and $\lambda_0 = 14$, which might need a finer spatial discretization to capture the narrower pressure spike. The convergence test for this case is shown in Fig. B1b. Again, the discretization used ($n_x = 2^{17}$ and $\Delta t/\Delta t_{max} = 50$) is sufficient in this case.

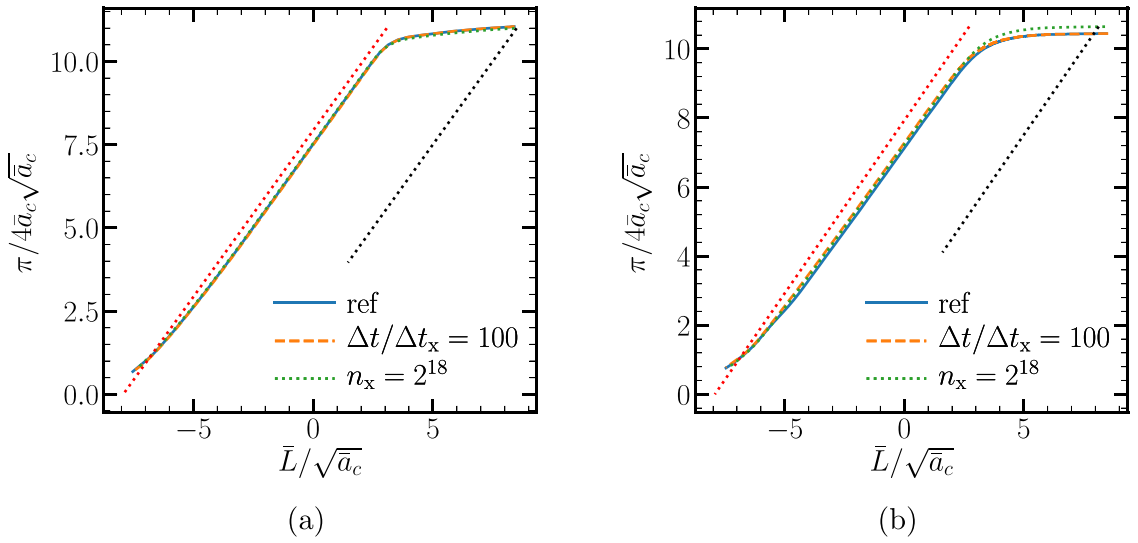

Fig. B1. Convergence test with increased spatial and temporal discretization. In (a), the reference case is given by $V_z = 4.5$, $\lambda_0 = 7$, $n_x = 2^{17}$ and $\Delta t/\Delta t_{max} = 50$. In (b), the reference case is given by $V_z = 0.9$, $\lambda_0 = 14$, $n_x = 2^{17}$ and $\Delta t/\Delta t_{max} = 50$. In the other cases, only the value indicated on the legend has been changed.

Appendix C. Non-dimensional formulation

The equations governing the contact problem are given by (14) and (4). Now, by using the scaled variables

$$X = \frac{x}{\beta} = \frac{x}{\left(R^2\Delta\gamma_0/E^*_0\right)^{1/3}}, \quad T = \frac{t}{\tau}, P = \frac{p}{\Delta\gamma_0/\Delta_{max}}, \quad U = \frac{u}{\beta^2/R}, \tag{C.1}$$

these equations may be written as.

$$\begin{aligned}
&P(Q,T) + \dot{P}(Q,T) = -8\left|Q\right|\frac{1}{\lambda_0}\left(U(Q,T) + \frac{1}{k}\dot{U}(Q,T)\right),\\
&G(X,T) = H_0(X) + VT - H_0(T) - U(X,T),\\
&G(X,T) = 0, \quad P(X,T) < 1,\\
&0 < G(X,T) \le \frac{1}{\lambda_0}, \qquad P(X,T) = 1,\\
&G(X,T) > \frac{1}{\lambda_0}, \qquad P(X,T) = 0,
\end{aligned} \tag{C.2a}$$

where $Q = q\beta$. In this case, the problem can be seen to be controlled by

$$\lambda_0 = \frac{\Delta\gamma_0}{\Delta_{max}}\left(\frac{R}{E^{*2}_0\Delta\gamma_0}\right)^{1/3}, \quad H_0 = \frac{h_0}{\Delta_{max}\lambda_\infty}, V = v_z\tau\left(\frac{E^{*2}_0}{\Delta\gamma_0^2 R}\right)^{1/3}, \quad k = \frac{E^*_0}{E^*_\infty} \tag{C.3}$$

Appendix D. Estimation of the width of the pressure spike

In order to estimate the width of the adhesive annulus, we need to estimate the value of m in (13). The dimensional version of that equation is [29].

$$\begin{aligned}
&\frac{a_a}{2R}\left(m\sqrt{m^2-1} - \operatorname{arccosh}(m)\right) +\\
&\frac{4p_a a_a}{\pi E*}\left(\sqrt{m^2-1}\operatorname{arccosh}(m) - m\log(m)\right) = \Delta_{max}.
\end{aligned} \tag{D.1}$$

This is a highly non-linear equation that cannot be solved analytically. To simplify it, we may note that, if the width of the adhesive annulus is much smaller than the contact area then $m \approx 1$. In this case, the following approximations hold,

$$\operatorname{arccosh}(m) \approx \sqrt(2)\sqrt{m-1}, \quad m\log(m) \approx (m-1). \tag{D.2}$$

Hence, we may approximate the first term in (D.1) as

$$\frac{a_a}{2R}\left(m\sqrt{(m-1)(m+1)}-\sqrt{2}\sqrt{m-1}\right)\approx \frac{a_a}{2R}\sqrt{2}\left(\left(m-1\right)\sqrt{(m-1)}\right), \tag{D.3}$$

and the second term as

$$\frac{4p_a a_a}{\pi E*}\left(\sqrt{(m+1)(m-1)}\sqrt{2}\sqrt{(m-1)}-(m-1)\right) \approx \frac{4p_a a_a}{\pi E*}(m-1). \tag{D.4}$$

Comparing these two terms, we see that when $m \to 1$, the first term will go faster to zero. Hence, we may neglect it to reach

$$\frac{4p_a a_a}{\pi E^*}(m-1) \approx \Delta_{\max}. \tag{D.5}$$

Finally, realizing that the width is given by $w = aa(m-1)$, we find

$$w = \frac{\pi E^* \Delta_{\max}}{4p_a}. \tag{D.6}$$

References

[1] Le Gal A, Klüppel M. Investigation and modelling of rubber stationary friction on rough surfaces. J Phys Condens Matter 2008;20(1).
[2] Lang A, Klüppel M. Influences of temperature and load on the dry friction behaviour of tire tread compounds in contact with rough granite. Wear 2017; 380–381:15–25.
[3] Krick BA, Vail JR, Persson BNJ, Sawyer WG. Optical in situ micro tribometer for analysis of real contact area for contact mechanics, adhesion, and sliding experiments. Tribol Lett 2012;45:185–94.
[4] Chopin J, Villey R, Yarusso D, Barthel E, Creton C, Ciccotti M. Nonlinear Viscoelastic modeling of adhesive failure for polyacrylate pressure-sensitive adhesives. Macromolecules 2018;51(21):8605–10.
[5] Robinson PW, Wheeler CA. The indentation rolling resistance of spherically profiled idler rolls. Int J Mech Sci 2016;106:363–71.
[6] Chen YL, Helm CA, Israelachvili JN. Molecular mechanisms associated with adhesion and contact angle hysteresis of monolayer surfaces. J Phys Chem 1991;95 (26):10736–47.
[7] Chaudhury MK, Weaver T, Hui CY, Kramer EJ. Adhesive contact of cylindrical lens and a flat sheet. J Appl Phys 1996;80(1):30–7.
[8] Baney JM, Hui CY. A cohesive zone model for the adhesion of cylinders. J Adhes Sci Technol 1997;11(3):393–406.
[9] Muller VM. On the theory of pull-off of a viscoelastic sphere from a flat surface. J Adhes Sci Technol 1999;13(9):999–1016.
[10] Vaenkatesan V, Li Z, Vellinga WP, de Jeu WH. Adhesion and friction behaviours of polydimethylsiloxane - A fresh perspective on JKR measurements. Polymer 2006; 47(25):8317–25.
[11] Waters JF, Guduru PR. Mode-mixity-dependent adhesive contact of a sphere on a plane surface. Proc R Soc A: Math Phys Eng Sci 2010;466(2117):1303–25.
[12] Lorenz B, Krick BA, Mulakaluri N, Smolyakova M, Dieluweit S, Sawyer WG, et al. Adhesion: role of bulk viscoelasticity and surface roughness. J Phys Condens Matter 2013;25(22).
[13] Tiwari A, Dorogin L, Bennett AI, Schulze KD, Sawyer WG, Tahir M, et al. The effect of surface roughness and viscoelasticity on rubber adhesion. Soft Matter 2017;13 (19):3602–21.
[14] Baek D, Hemthavy P, Saito S, Takahashi K. Evaluation of energy dissipation involving adhesion hysteresis in spherical contact between a glass lens and a PDMS block. Appl Adhes Sci 2017;5(4):1–11.
[15] Dalvi S, Gujrati A, Khanal SR, Pastewka L, Dhinojwala A, Jacobs TD. Linking energy loss in soft adhesion to surface roughness. Proc Natl Acad Sci USA 2019;116 (51):25484–90.
[16] Johnson KL, Kendall K, Roberts AD. Surface energy and the contact of elastic solids. Proc R Soc Lond Ser A 1971;324:301–13.
[17] Carbone G, Pierro E, Recchia G. Loading-unloading hysteresis loop of randomly rough adhesive contacts. Phys Rev E - Stat Nonlinear Soft Matter Phys 2015;92(6): 1–8.
[18] Violano G, Afferrante L. Adhesion of compliant spheres: an experimental investigation. Procedia Struct Integr 2019;24(2019):251–8.
[19] Greenwood JA, Johnson KL. The mechanics of adhesion of viscoelastic solids. Philos Mag A: Phys Condens Matter Struct Defects Mech Prop 1981;43(3):697–711.
[20] Persson BNJ, Brener EA. Crack propagation in viscoelastic solids. Phys Rev E - Stat Nonlinear Soft Matter Phys 2005;71(3):1–8.
[21] Carbone G, Persson BNJ. Crack motion in viscoelastic solids: the role of the flash temperature. Eur Phys J E 2005;17(3):261–81.
[22] Barthel E, Frétigny C. Adhesive contact of elastomers: effective adhesion energy and creep function. J Phys D: Appl Phys 2009;42(19).
[23] Van Dokkum JS, Nicola L. Green's function molecular dynamics including viscoelasticity. Model Simul Mater Sci Eng 2019;27(7).
[24] Carbone G, Putignano C. A novel methodology to predict sliding and rolling friction of viscoelastic materials: theory and experiments. J Mech Phys Solids 2013; 61(8):1822–34.
[25] Bugnicourt R, Sainsot P, Lesaffre N, Lubrecht AA. Transient frictionless contact of a rough rigid surface on a viscoelastic half-space. Tribol Int 2017;113:279–85.
[26] S.C.P. Marques, G.J. Creus, Computational Viscoelasticity, 2012.
[27] Dugdale D. Yielding of steel sheets containing slits. J Mech Phys Solids 1960;8(2): 100–4.
[28] Maugis D. Adhesion of spheres: the JKR-DMT transition using a dugdale model. J Colloid Interface Sci 1992;150(1):243–69.
[29] Johnson KL, Greenwood JA. Maugis analysis of adhesive line contact (Journal of Physics D: Applied Physics (2008) 41 (155315)). J Phys D: Appl Phys 2008;41(19).
[30] Derjaguin BV, Muller VM, Toporov YP. Effect of contact deformations on the adhesion of particles. J Colloid Interface Sci 1975;53(2):314–26.
[31] Störmer C. Sur les trajectoires des corpuscules électrisés dans laespace sous laaction du magnétisme terrestre, avec application aux aurores boréales. Le Radium 1912;9(11):395–9.
[32] Johnson KL. Contact Mechanics. The Press Syndicate of the University of Cambridge; 1985.
[33] Dorogin L, Tiwari A, Rotella C, Mangiagalli P, Persson BNJ. Role of preload in adhesion of rough surfaces. Phys Rev Lett 2017;118(23):1–6.
[34] Persson BNJ, Albohr O, Heinrich G, Ueba H. Crack propagation in rubber-like materials. J Phys Condens Matter 2005;17(44).
[35] Frigo M, Johnson SG. The design and implementation of FFTW3. Proc IEEE 2005; 93(2):216–31.